

Vat photopolymerization of ultra-porous bioactive glass foams

Original

Vat photopolymerization of ultra-porous bioactive glass foams / Baino, F.; Gaido, F.; Gabrieli, R.; Alidoost, D.; Schiavi, A.; Mohammadi, M.; Schwentenwein, M.; Tulyaganov, D.; Verne', E.. - In: OPEN CERAMICS. - ISSN 2666-5395. - ELETTRONICO. - 20:(2024). [10.1016/j.oceram.2024.100690]

Availability:

This version is available at: 11583/2994373 since: 2024-11-13T16:42:38Z

Publisher:

Elsevier

Published

DOI:10.1016/j.oceram.2024.100690

Terms of use:

This article is made available under terms and conditions as specified in the corresponding bibliographic description in the repository

Publisher copyright

(Article begins on next page)



Vat photopolymerization of ultra-porous bioactive glass foams

Francesco Baino^{a,*}, Federico Gaido^a, Roberta Gabrieli^a, Dario Alidoost^{a,b}, Alessandro Schiavi^c, Mehdi Mohammadi^d, Martin Schwentenwein^d, Dilshat Tulyaganov^e, Enrica Verné^a

^a Institute of Materials Physics and Engineering, Department of Applied Science and Technology, Politecnico di Torino, 10129, Turin, Italy

^b J-Tech Interdepartmental Research Centre, Politecnico di Torino, Corso Duca Degli Abruzzi 24, 10129, Turin, Italy

^c National Institute of Metrological Research (INRIM), Applied Metrology and Engineering Division, 10135, Turin, Italy

^d Lithoz GmbH, Vienna, Austria

^e Department of Natural-Mathematical Sciences, Turin Polytechnic University in Tashkent, Tashkent, 100095, Uzbekistan

ARTICLE INFO

Handling Editor: Jens Guenster

Keywords:

Bioactive glass
Scaffold
3D printing
Porosity
Bone

ABSTRACT

The introduction of additive manufacturing technologies in the field of biomaterials science has opened new horizons for regenerative medicine. In this work, we pushed the potential of vat polymerization to the limit for fabricating ultra-porous bioactive $\text{SiO}_2\text{-CaO-MgO-P}_2\text{O}_5\text{-CaF}_2\text{-Na}_2\text{O}$ glass scaffolds with bone-like architectural characteristics. The tomographic reconstruction of an open-cell foam was used as input file to the printing system and reliably reproduced in all its exquisite details, as assessed by morphological analyses of sintered scaffolds (thickness of single struts 35 μm , exceptionally high porosity around 94 vol%, most pores with size from 500 to 900 μm). Immersion studies in simulated body fluid (SBF) revealed the apatite-forming ability (i.e., *in vitro* bioactivity) of the scaffolds, the surface of which started being coated by calcium phosphate after just 3 days from the beginning of the experiments. Taken together, these results show great promise for application of such scaffolds in bone defect repair.

1. Introduction

Bioactive glasses have been routinely used in the clinic since the mid 1990s in a plenty of bone-contact applications, including the repair of small osseous defects in orthopaedics and maxillofacial surgery, lost volume filling in vertebroplasty, and alveolar bone regeneration in dentistry [1–3]. A few millions of patients have benefitted from the appealing properties of bioactive glasses, which are not only able to bond to living bone creating a strong interface (osteoconduction) but also to stimulate bone cells towards paths of bone regeneration through the release of osteostimulatory ionic dissolution products (osteinduction), thereby ultimately boosting tissue self-repair [4,5]. These attractive characteristics have made bioactive glasses ideal candidates for bone tissue engineering applications, which typically require the use of a porous biomaterial (“scaffold”) supporting and even stimulating the growth of newly-formed tissue in three-dimensions (3D) inside the patient’s body [6]. Furthermore, being inherently osteoinductive, bioactive glass scaffolds do not necessarily need pre-seeding with cells prior to being implanted in the host bone [7].

Additive manufacturing of biomaterials has significantly contributed

to the recent progress in the field [8], allowing porous structures to be fabricated with a high control on internal characteristics and reproducibility, which is key in view of reliability and industrial scalability. Bioactive glasses can indeed be processed by 3D-printing approaches: for example, just to cite a couple of clinically-approved formulations, 13–93 glass scaffolds were produced by selective laser sintering [9], while 45S5 Bioglass® scaffolds were manufactured by robocasting [10] or vat photopolymerization [11]. Extrusion-based technologies such as robocasting, despite requiring a more affordable equipment compared to the other methods, typically suffer from the limitation of having filaments of glass-containing ink as “structural units” for the scaffold, yielding to the production of “rectilinear” grids that can be overlapped with different orientations but do not properly mimic the foam-like architecture of bone in 3D. This drawback has been recently overcome with the vat photopolymerization of bioactive silicate glass scaffolds (composition “47.5B”) using the tomographic reconstruction of an open-cell polyurethane foam (CAD file) as the input to the printing machine (CAM system) [12]. The same approach was also adopted to fabricate hydroxyapatite scaffolds [13], with promising results from the viewpoints of mechanical properties and printing fidelity [14].

* Corresponding author.

E-mail address: francesco.baino@polito.it (F. Baino).

<https://doi.org/10.1016/j.oceram.2024.100690>

Received 2 August 2024; Received in revised form 20 September 2024; Accepted 30 September 2024

Available online 30 September 2024

2666-5395/© 2024 The Authors. Published by Elsevier Ltd on behalf of European Ceramic Society. This is an open access article under the CC BY license (<http://creativecommons.org/licenses/by/4.0/>).

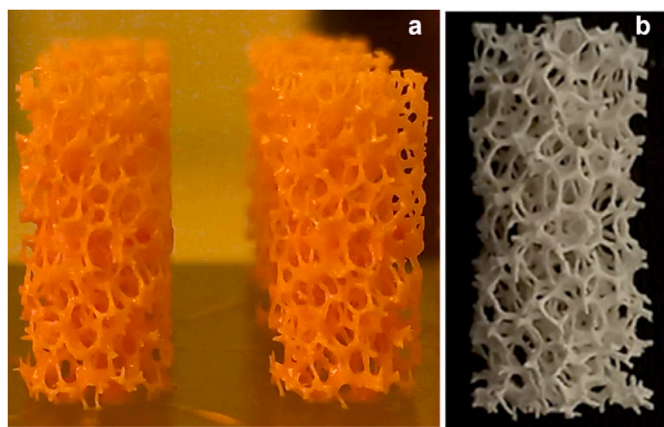


Fig. 1. Results of the printing process: (a) cleaned greens; (b) sintered scaffold (diameter around 5.70 mm, height around 12.50 mm).

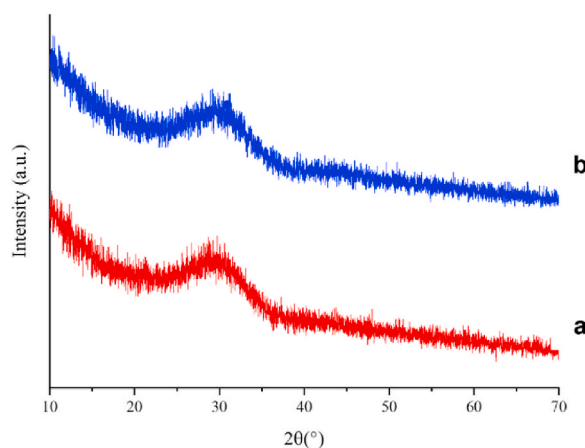


Fig. 2. XRD patterns of (a) initial BG-1d powder and (b) pulverized scaffold after sintering at 700 °C.

One of the key requirements for bone-tissue engineering scaffolds is the high porosity, which allows the biological fluids to flow in and out, the newly-formed bone to grow in and the blood vessel to mature inside the implant [15]. However, to the best of the authors' knowledge, total porosity exceeding 80 vol% is difficult to achieve – for bioceramic products in general – owing to problems of mechanical integrity of the sintered parts. In this work, using the promising results achieved in Ref. [12] with the glass 47.5B as a starting point, we pushed the potential of digital light processing (DLP)-based vat photopolymerization to the limit in order to produce ultra-porous scaffolds from the bioactive glass “1d” (BG-1d), going well beyond the threshold of 80 vol% porosity. This material (compositional system $\text{SiO}_2\text{--P}_2\text{O}_5\text{--CaO--MgO--Na}_2\text{O--CaF}_2$) has not been approved yet for routine clinical use but showed superior biocompatibility and comparable osteoinductive properties *in vitro* with respect to 45S5 Bioglass® used as a standard reference [16]. Furthermore, excellent bone-regeneration ability was reported upon implantation of BG-1d particulate to treat jawbone defects in 45 human patients after cystectomy [17]. Given these promising results, BG-1d was considered a highly appealing biomaterial for the production of bone-tissue engineering highly-porous scaffolds.

Therefore, this work exhibits two elements of novelty compared to the current state of the art: (i) for the first time the bioactive glass 1d is used as a material for producing scaffolds by an additive manufacturing technology (i.e., vat photopolymerization), and (ii) also for the first time so exceptionally-porous glass products (>94 vol% of empty space) were fabricated by applying this manufacturing method, thus extending its

boundaries of usage.

2. Materials and methods

2.1. Preparation of glass

BG-1d glass (composition 46.1SiO₂-28.7CaO-8.8MgO-6.2P₂O₅-5.7CaF₂-4.5Na₂O wt.% [18]), selected for scaffold fabrication, was produced by melt-quenching method using high-purity reagents (SiO₂, CaCO₃, 4MgCO₃·Mg(OH)₂·5H₂O, NH₄H₂PO₄, CaF₂, Na₂CO₃), all purchased from Merck. After being carefully mixed according to the compositional ratios, the reagent powders were homogeneously mixed in a plastic bottle onto rotating rollers overnight to promote the homogeneity of the mix and were then put inside a platinum crucible at room temperature. The powder mix was hand-pressed to reduce the air inside the blend to minimum and the crucible was then put inside an electrically-heated furnace (Nabertherm GmbH, Germany) to reach melting at 1450 °C. After 1 h, melt was quenched in cold water at room temperature to produce the “frit”, which was dried and ball milled in a planetary milling machine with six zirconia spheres (Pulverisette 6, Fritsch, Germany). Particles were sieved below 25 µm using a stainless-steel sieve (Giuliani Technologies Srl, Torino, Italy) introduced inside a sieve shaker (Octagon 200, Endecott's, England). According to previous knowledge, this particle size could be suitable to produce porous glass scaffolds by vat photopolymerization.

2.2. Fabrication of scaffolds

Powder of BG-1d was homogeneously dispersed in a photocurable resin produced by Lithoz, consisting of acrylates and methacrylates with a photoinitiator and dispersing additive in order to prevent aggregation and sedimentation phenomena in the slurry. Scaffolds were fabricated using a DLP-based vat photopolymerization 3D printing system (CeraFab 7500, Lithoz GmbH, Vienna, Austria), which utilizes a LED light in the blue range of the electromagnetic spectrum to cure the glass-containing resin.

In line with previous studies, a CAD file created from micro-CT scan of a 45-ppi commercial polyurethane sponge cuboid was utilized as a virtual template to fabricate cylindrical porous scaffolds with a final architecture resembling that of cancellous bone [13]. Specifically, a parallelepiped was obtained by stacking a copy of the CT-scanned cubic sponge on top of the original, then, a circle was inscribed inside the square base of the parallelepiped to extrude a porous cylinder with a 2:1 aspect ratio.

Given the shrinkage effect during scaffold sintering, shrinkage compensation factors of 1.55 for the XY plane and 1.6 for the Z axis were considered. No contour offset was applied in this study; such parameter is commonly used to increase the thickness of the struts of the green body, simplifying the printing process and enhancing the structural integrity [13], and setting it to zero we aimed at generating ultra-porous structures.

During the printing, each scaffold was divided in 641 layers; the print layer thickness was 25 µm and the entire printing process took approximately 23 h. Every printing job involved the fabrication of eighteen scaffolds simultaneously. Once the job ended, the printed parts were removed from the building platform of the printer and then, in order to remove excess non-polymerized slurry, the green bodies underwent two ultrasonic baths with LithaSol 80 (Lithoz GmbH, Vienna, Austria), which is an organic-based solution for cleaning ceramic green bodies. Cleaned greens were thermally treated in the same electrical furnace (Nabertherm P330, Nabertherm GmbH, Germany) for ensuring consistent experimental conditions. During sintering, in order to have the most homogenous temperature profile in the oven, the scaffolds were placed inside a case with a lid which, through holes on the sides, allowed the gases to escape from it without being trapped inside. The maximum temperature reached was 700 °C for 1 h; the whole sintering

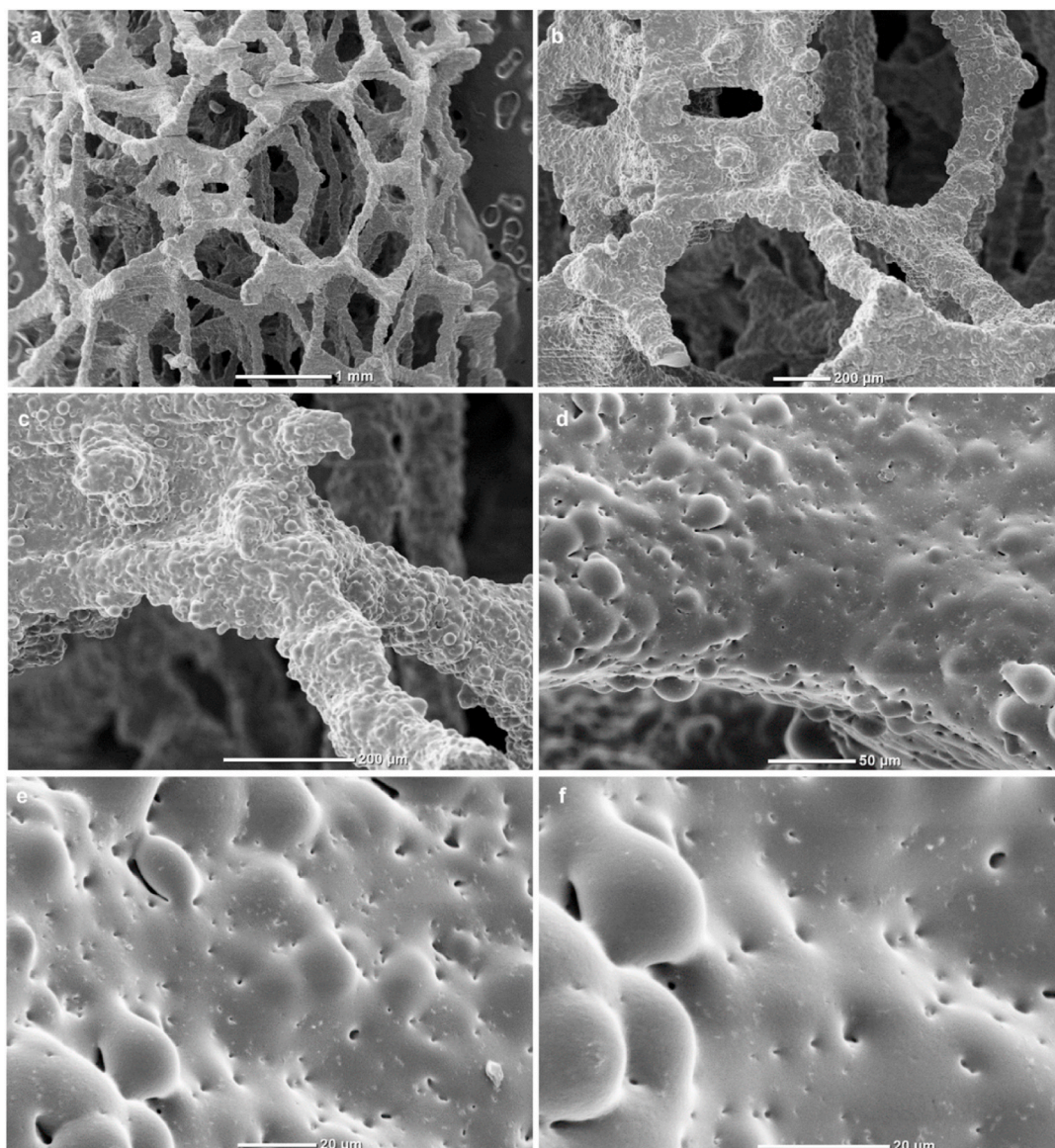


Fig. 3. SEM micrographs showing the 3D ultra-porous architecture and strut surface of scaffolds at different magnifications: (a) 22 \times , (b) 65 \times , (c) 150 \times , (d) 400 \times , (e) 900 \times , (f) 1500 \times .

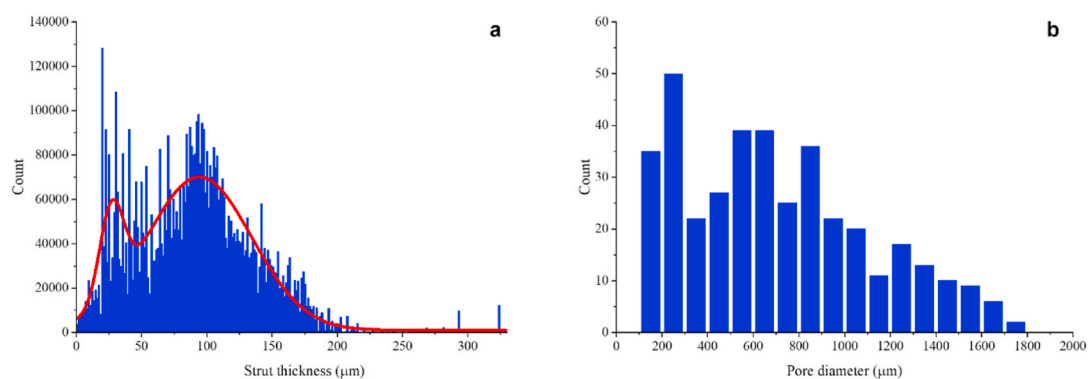


Fig. 4. Results from micro-CT analysis on BG-1d scaffolds: distributions of (a) strut thickness and (b) pore size (diameter).

process lasted approximately 53 h. Selection of this sintering treatment was also based on thermal analyses reported in previous studies [18–21].

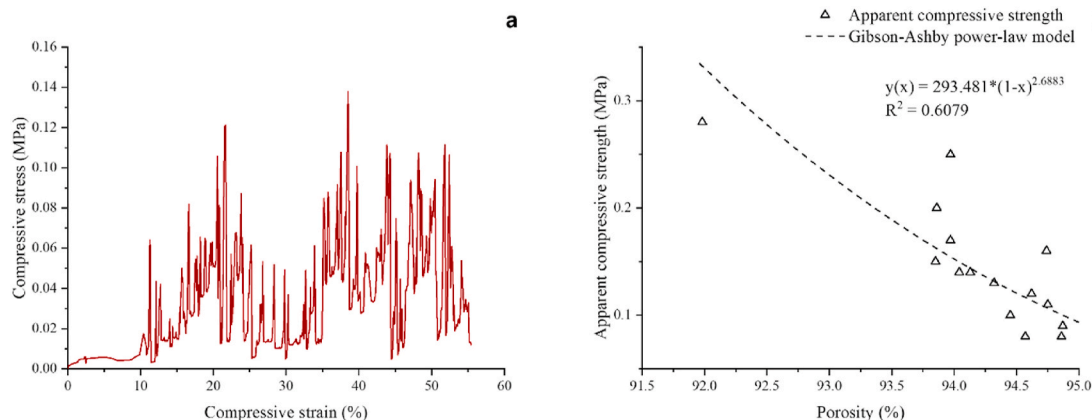


Fig. 5. Results from mechanical tests: (a) example of a typical stress-strain curve and (b) modelling of experimental data.

2.3. Characterizations

2.3.1. Microstructure

X-ray diffraction (XRD) was performed both on as-produced BG-1d powders after melting/crushing/sieving and on BG-1d-derived scaffolds after pulverization by ball milling (Pulverisette 0, Fritsch GmbH, Germany). XRD analysis was performed in the 2 θ -range of 10–70° by using the diffractometer X'Pert Pro PW3040/60 (PANalytical, Eindhoven, The Netherlands) with the following experimental conditions: Bragg-Brentano camera geometry, Cu K α incident radiation (wavelength λ = 0.15405 nm), voltage 40 kV, filament current 40 mA, angular step size 0.02°, fixed counting time per step 1 s. The data from the obtained XRD patterns were analysed by making use of the X-Pert HighScore Software and ICDD PDF database.

2.3.2. Porosity and morphology

The surface characteristics and overall pore-strut architecture of sintered scaffolds were investigated by scanning electron microscopy (SEM, JCM-6000Plus benchtop SEM, JEOL, Tokyo, Japan) at an accelerating voltage of 5 kV. Samples were sputtered with platinum prior to the analysis.

The total porosity (vol%) of the scaffolds was determined as $(1 - \rho/\rho_0) \times 100$, where ρ is the bulk density of the scaffold (calculated as the mass-to-volume ratio) and ρ_0 is the density of the solid skeleton (solid struts). Result was expressed as average \pm standard deviation calculated on 20 specimens. Massive 1d-derived samples were printed, subjected to the same heat treatment adopted for making scaffolds (700 °C for 1 h) and finally used to determine ρ_0 through the use of the Archimedes' principle, special scales and a Sartorius density determination kit YDK 01. Specifically, the density of the solid was calculated as $\rho_0 = \frac{W_a(\rho_l - \rho_a)}{\rho_w(W_a - W_l)} + \rho_a$, which incorporates variables such as the weight in liquid (W_l) and in air (W_a) of solid samples sintered at the same temperature as the ultra-porous scaffolds, the density of water at a temperature of 22.5 °C ($\rho_w = \rho_l = 0.9977735$ g/cm³) and the density of air $\rho_a = 0.001225$ g/cm³. Finally, the value of density of thermally-treated, 3D-printed "solid" BG-1d was $\rho_0 = 2.845 \pm 0.033$ g/cm³.

A more detailed quantification of pore features was performed by micro-computed tomography (micro-CT) using a custom-made equipment available in the Interdepartmental Centre "J-Tech" at Politecnico di Torino. A proper internal sub-volume of the scaffold was selected to avoid artefacts related to the outer surface. Projection images were collected using a source voltage of 50 kV and a source current of 200 μ A, along with a source-to-object distance of 40 mm and a source-to-detector distance of 800 mm. No filter was used and the voxel size was 10 μ m. Angular rotation step was 0.225°, exposure time was 1 s per projection. Post-processing and quantitative analyses were performed through VGStudio MAX software.

2.3.3. Mechanical strength

Scaffolds underwent uniaxial compression perpendicularly to the bases of the porous cylinder. The compressive strength (σ , expressed in MPa) was calculated as the ratio $\frac{F}{A_0}$, where F is the peak load (expressed in N) recorded during the test and A_0 is the initial contact surface (i.e., the resistant cross-sectional area, expressed in mm²). This test was performed on 15 scaffolds by using a custom-made stress-strain testing machine, available in INRiM (details can be found in Ref. [22]), comprising a 50 N load cell with a resolution of 0.1 mN and a digital displacement sensor with a resolution of 0.1 μ m to measure the cross-head displacement (the crosshead speed was set at 0.5 mm/min, corresponding to a strain rate of 0.001 s⁻¹).

2.3.4. In vitro mineralization

The bioactive properties of scaffolds were studied, in terms of in vitro apatite-forming ability, by immersion in a simulated body fluid (SBF) prepared according to the Kokubo and Takadama's protocol [23]. Triplicate tests were carried out for five different periods of time (24 h, 48 h, 72 h, 7 days and 14 days) under dynamic controlled conditions inside an orbital shaker (rotational velocity 100 rpm, temperature 37 °C) without any refresh of the solution. The mass (scaffold)-to-liquid (SBF) ratio was fixed to 1.5 mg/mL, as commonly adopted for in vitro bioactivity studies in SBF when specimens with high surface area are tested [24], such as the highly porous scaffolds investigate in this work. The solution pH was recorded every 48 h or, for timepoints shorter than then 48 h, at the end of the experiments.

After being crushed to obtain fine powders, the SBF-treated scaffolds underwent XRD analysis according to the set-up reported in section 2.3.1 in order to detect the presence of newly-formed phases (mineralization).

Morphological analyses by SEM, equipped with energy-dispersive spectroscopy (EDS) for compositional analysis, were also performed using the same experimental conditions already described in section 2.3.2.

SBF-treated scaffolds were finally non-destructively analysed by micro-CT to further analyse the characteristics of the reaction layer formed on the struts.

3. Results and discussion

The printing procedure allowed the successful fabrication of glass replicas of the virtual spongy template. Despite being apparently very delicate because of the ultra-high porosity, the green sample could be manipulated after printing without undergoing any damage (Fig. 1a); the orange colour was due to the presence of the resin that will be removed during thermal debinding. An example of sintered scaffold is shown in Fig. 1b. The diameter and height of porous cylinders,

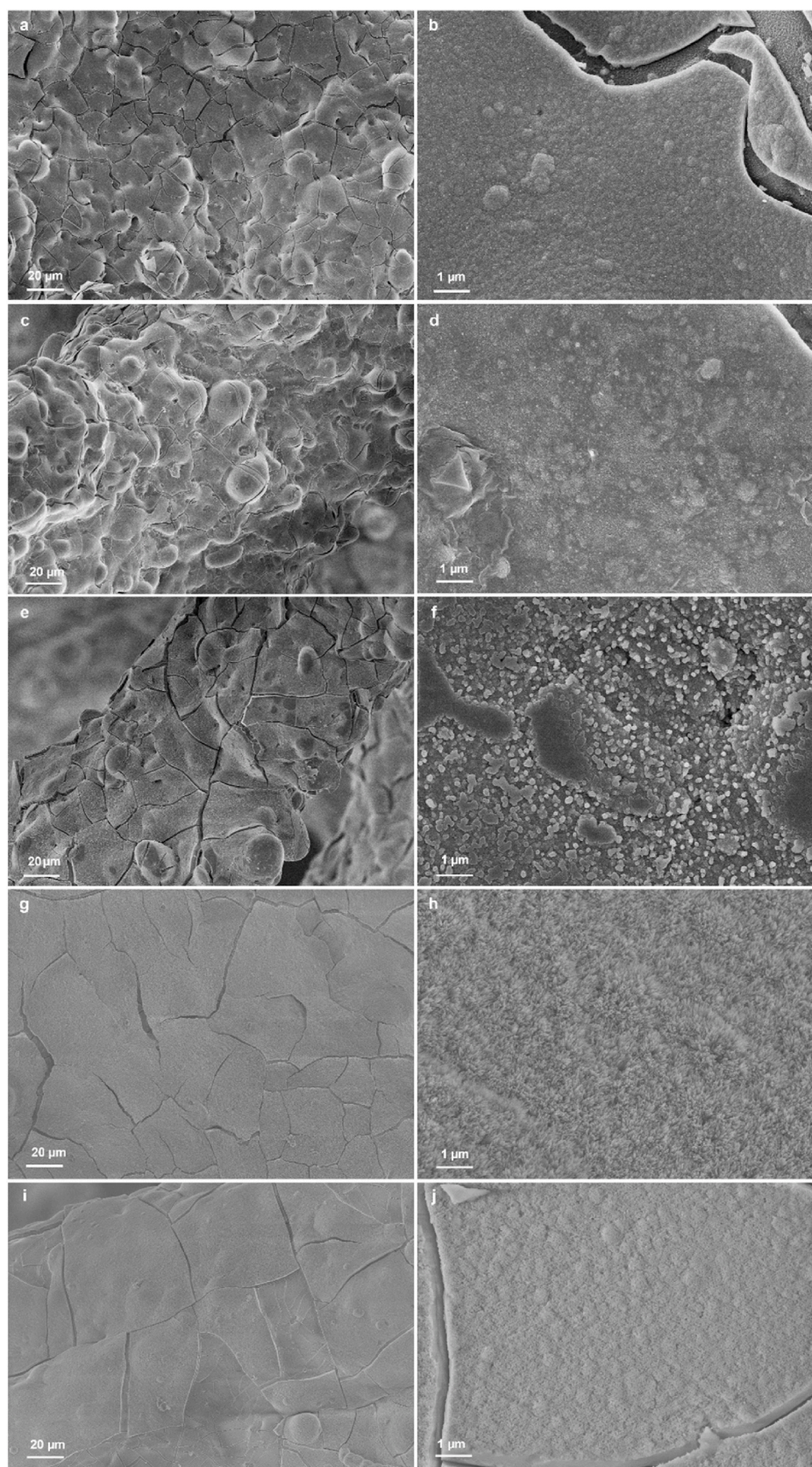


Fig. 6. In vitro bioactivity of BG-1d scaffolds: SEM micrographs of strut surface after immersion in SBF for (a,b) 24 h, (c,d) 48 h, (e,f) 72 h, (g,h) 7 days and (i,j) 14 days. Images on the left column: magnification $1000\times$; images on the left column: magnification $20,000\times$.

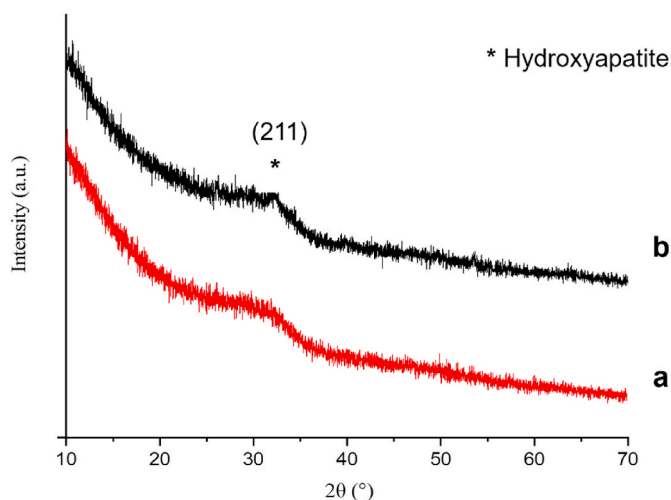


Fig. 7. XRD analysis on BG-1d scaffolds after immersion in SBF for (a) 7 days and (b) 14 days.

calculated on 20 specimens, were 5.72 ± 0.083 mm and 12.49 ± 0.94 mm, respectively, with ratios of standard deviation to average of 1.5 % and 7.5 % for these two geometrical dimensions, revealing a good reproducibility of the printing process.

Fig. 2 shows the XRD patterns obtained for the BG-1d powder (after being melted, crushed and sieved) and sintered scaffold (after being pulverized), indicating that the heat treatment did not induce any microstructural variations. In fact, both XRD patterns displayed an amorphous halo located at low scattering angles ($\sim 25\text{--}35^\circ$), which is typical of silicate glasses. The absence of any crystalline phase in the scaffold is due to the fact that the sintering temperature (700°C) is lower than the crystallization temperature (T_c) previously assessed through DTA of BG-1d powder.

The total porosity of scaffolds was 94.0 ± 0.7 vol% (range from 91.4 to 95.2 vol%); to the best of the authors' knowledge, this is the highest value of porosity ever obtained for bioactive glass scaffolds regardless of the fabrication method adopted [6]. Although being exceptionally high, the porosity of BG-1d scaffolds still falls in the typical range of cancellous bone range (75–95 vol%) (very close to the upper limit) [25].

Morphological investigations, as depicted in Fig. 3, confirm that the 3D pore-strut architecture of the scaffolds closely replicates the cellular structure of the virtual model (polymer sponge) and, thus, effectively mimics the architecture of trabecular bone. Notably, the profile of the original glass particles can be observed on the surface of the trabeculae because of incomplete sintering. Hence, micrometric pores can be observed on the surface of scaffold struts, resulting from the interparticle voids mentioned above as well as the release of gases during thermal

treatment [26]. Densification of struts could indeed be improved by increasing the sintering temperature above 700°C and/or the sintering time, especially to increase the mechanical properties; on the other hand, however, this surface topography is beneficial from a biological viewpoint as osteoblasts preferably spread on micro-rough bone implants [27].

The micro-CT analysis allows assessing the strut thickness distribution (Fig. 4a), which exhibited two main peaks. Therefore, trabecular thicknesses (diameters) followed a bimodal distribution instead of a Gaussian one, which can be mainly attributed to the crossing or overlapping of scaffold struts. Hence, the first peak in Fig. 4a corresponds to the actual thickness of single trabeculae, while the second peak is due to the “intersection” and “merging” of scaffold struts. A similar trend has also been reported in a previous work dealing with hydroxyapatite scaffolds produced by the same 3D-printing method [28].

In our study, the first peak is around $35\text{ }\mu\text{m}$ and the second appears at approximately $100\text{ }\mu\text{m}$. Moreover, trabeculae with diameters less than $1.3\text{ }\mu\text{m}$ and greater than $324.1\text{ }\mu\text{m}$ were not found. These values yield an average strut thickness of $90.2\text{ }\mu\text{m}$ with a standard deviation of $47.2\text{ }\mu\text{m}$.

The micro-CT analysis also includes the assessment of pore size distribution throughout the scaffold (Fig. 4b). The absence of pores below $100\text{ }\mu\text{m}$ can be attributed to the exceptionally high porosity of the virtual template used for scaffold printing. The minimum and maximum diameters of pores are around 175 and $1800\text{ }\mu\text{m}$, respectively, and the average pore size was $801\text{ }\mu\text{m}$; most pores are in the range of $500\text{--}900\text{ }\mu\text{m}$ with a noticeable decreasing amount as pore size increases.

An example of compressive stress-strain curve for BG-1d scaffolds sintered at 700°C for 1 h is shown in Fig. 5a, revealing the typical behaviour of highly porous ceramic of glass foams. Such structures tend to crack first in thin struts at stress-concentrating sites, causing the apparent stress to drop temporarily; however, the whole scaffold can still withstand higher loads, causing the stress to rise again, and the repetition of the cracking of struts yields a jagged stress-strain curve [29]. The profile of the curve displayed in Fig. 5a is also very similar to the result reported by Chen et al. [30], who tested 45S5 Bioglass® foams with approximately 90 vol% porosity: first, there is an initial phase where the curve has an overall positive slope until a major peak is reached (strain around 21 %); this maximum stress causes the thick struts of the BG-1d scaffold to fracture and then a significantly negative slope occurs; finally, stress increases again (starting from strain around 35 %) as densification of fractured struts occurred.

Fig. 5b illustrates that the apparent compressive strength is dependent on scaffold porosity: as the total porosity increases, mechanical strength decreases significantly. Specifically, the compressive strength is in the range of 0.08 MPa for the most porous scaffold tested in this work (94.9 vol%) to 0.28 MPa (porosity 92.0 vol%). This result was predictable, as an increase in porosity inevitably leads to a smaller volume occupied by the material under examination, resulting in reduced resistance to compressive loads. Fig. 5b also includes data interpolation

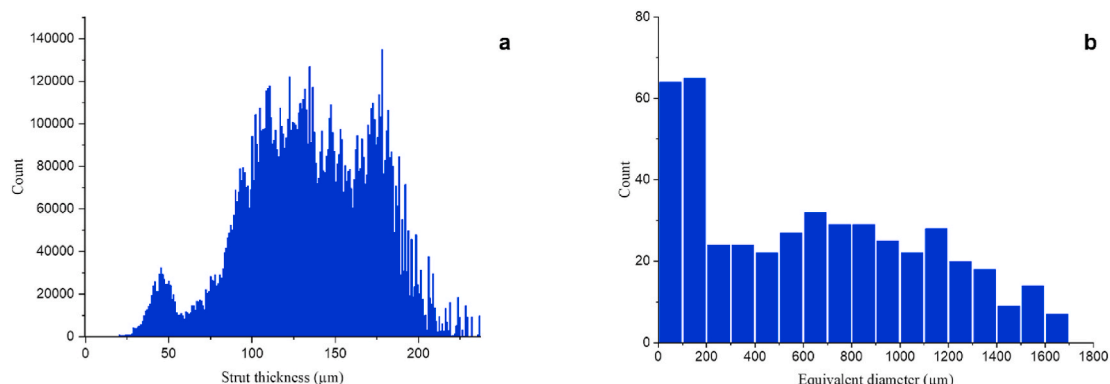


Fig. 8. Results from micro-CT analysis on BG-1d scaffolds after immersion for 14 days in SBF: distributions of (a) strut thickness and (b) pore size (diameter).

using the Gibson-Ashby power-law model (Equation (4)), which is commonly employed to describe the dependence of mechanical strength on porosity in porous solids with foam-like architecture [31]:

$$\sigma = \sigma_0 C_1 (1 - p)^b \quad (4)$$

The fitting of experimental data to determine the model parameters $a = \sigma_0 C_1$ and b (see Fig. 5b) was carried out using a proper code developed in MATLAB® based on the least squares method. The coefficient $R^2 = 0.6079$ suggests an acceptable accuracy and fair predictive capability of the power-law model for the compressive strength. Other authors [15] proposed a simple linear interpolation to model the strength-porosity data from highly porous 45S5 glass foams (porosity around 90 vol%), but the results obtained in that work were completely unsatisfactory ($R^2 = 0.087$) probably because of the high dispersion of experimental points and poor reproducibility of those scaffolds that were not fabricated by 3D printing.

During the in vitro bioactivity tests, the pH of SBF showed a constant increase over time until the seventh day. From this point onward, the pH value remained constant at 7.59 ± 0.02 . Compared to the study conducted by Tulyaganov et al. [17], the plateau pH value (around 7.60 also in this case) is reached much more quickly in the present work due to the high porosity of the scaffolds. In fact, by increasing the surface area of the material exposed to SBF, the reaction rate and efficiency inevitably increase. The pH of the solution remains moderately alkaline, which is beneficial to promote bone cell viability and osteogenesis; on the contrary, excessively alkaline pH levels (>7.9) make osteogenic differentiation of human bone marrow mesenchymal stem cells impossible, creating a hostile biological microenvironment [32]. In BG-1d, the presence of fluoride ions prevents a significant increase of pH values: in fact, instead of being replaced with H^+ ions, fluoride ions are replaced by hydroxyl ions (OH^-) and, consequently, the pH of SBF containing BG-1d is lower than, for example, that of SBF with Bioglass® [16].

The in vitro apatite-forming ability of BG-1d granules [17] and porous scaffolds produced by conventional foam-replica method [21] was comprehensively studied elsewhere. In order to corroborate these previous results, some relevant analyses were also carried out on the novel 3D-printed BG-1d scaffolds investigated in the present work. Fig. 6 shows the evolution of scaffold struts upon immersion experiments in SBF. After just 1 day in the solution, the presence of a silica gel layer on the surface of the trabeculae is well visible, in perfect agreement with the bioactivity mechanism proposed by Hench for silicate bioactive glasses [33]. The thickness of this layer increases over time eventually evolving in a calcium phosphate coating, as confirmed by compositional analysis by EDS, that completely lines the struts. Cracking of the silica gel layer is due to the drying of the scaffold and the high vacuum applied in the chamber of SEM equipment. The EDS analysis reveals that the presence of silicon remains high after 24 h and 48 h, consistently with the formation of the silica gel layer on the surface of scaffold trabeculae (first stage of the bioactivity mechanism). The content of silicon on the scaffold surface progressively diminishes in the subsequent 3 timesteps (72 h, 7 days and 14 days), concurrently to the formation of the calcium phosphate layer. Calcium phosphate nuclei were clearly detected on the top of silica gel after 72 h, followed by the progressive formation of globular agglomerates with the typical morphology of bone-like hydroxyapatite. The Ca/P atomic ratio, assessed by EDS analysis, was determined to be 1.82, 2.34 and 2.64 after 72 h, 7 days and 14 days, respectively. A reliable quantification of Ca and P was not possible due to the overlapping between the peaks of phosphorus, contained in the newly-formed layer, and platinum, used for the metal-sputtering of the samples prior to the analysis. However, the increasing trend of the Ca/P ratio suggests an enrichment in Ca of the top layer, in agreement with the formation of surface hydroxyapatite [34]. The nature of this newly-formed phase was confirmed by XRD analysis (Fig. 7): although after immersion in SBF for 1 week no significant changes were observed compared to the untreated material, a broad diffraction peak around 32°

- which is the typical fingerprint of nano-crystalline hydroxyapatite formed on the surface of bioactive glasses - can be clearly detected after 14 days. This finding is consistent with previous results reported for BG-1d granules soaked in SBF [17].

The micro-CT analysis of the sample soaked for 14 days in SBF (Fig. 8) showed an increase in strut thickness compared to the untreated scaffold. The two peaks in the trabecular thickness distribution shifted from 35 to 50 μm (first peak) and from 100 μm to a range between 130 and 190 μm (second peak). This increase in thickness is due to the formation of the hydroxyapatite layer on the surface of struts during immersion in SBF, which is consistent with the SEM observations reported in Fig. 6. As a consequence of the increased trabecular thickness, the pores sizes become smaller; in fact, the dimensional pore range is reduced to 70–1650 μm and the mean diameter assessed after immersion in SBF is 643 μm , which is significantly lower than the value obtained before the in vitro bioactivity experiments (801 μm).

4. Conclusions

Vat photopolymerization proved to be successful and reliable in producing exceptionally porous foam-like scaffolds (total porosity 94 vol%) starting from a silicate bioactive glass. To the best of the authors' knowledge, these scaffolds are the most porous ones that have been ever obtained till now using bioceramic or glass materials and, probably, one of most porous products ever obtained by an additive manufacturing technology. The samples exhibit bone-like characteristics and apatite-forming ability upon immersion in SBF. Besides the specific significance in the field of bone biomaterials, this work expands the potential of additive manufacturing applied to glasses and ceramics, opening new horizons in a myriad of advanced and high-tech applications requiring ultra-porous structures such as catalysis, phase separation, thermal insulation, construction, aerospace and lightweight materials.

CRedit authorship contribution statement

Francesco Baino: Writing – review & editing, Writing – original draft, Validation, Supervision, Resources, Project administration, Methodology, Investigation, Conceptualization. **Federico Gaido:** Writing – original draft, Methodology, Investigation, Data curation. **Roberta Gabrieli:** Writing – review & editing, Methodology, Investigation, Data curation. **Dario Alidoost:** Methodology, Investigation, Data curation. **Alessandro Schiavi:** Writing – review & editing, Resources, Methodology, Investigation, Data curation. **Mehdi Mohammadi:** Writing – review & editing, Methodology, Investigation, Data curation. **Martin Schwentenwein:** Writing – review & editing, Supervision, Resources, Methodology, Conceptualization. **Dilshat Tulyaganov:** Writing – review & editing, Methodology, Conceptualization. **Enrica Verné:** Writing – review & editing, Supervision, Resources, Methodology, Conceptualization.

Declaration of competing interest

The authors declare that they have no known competing financial interests or personal relationships that could have appeared to influence the work reported in this paper.

Acknowledgements

This study was carried out within the «Artificial Intelligence-based design of 3D PRINTed scaffolds for the repair of critical-sized BONE defects - I-PRINT-MY-BONE (CUP: E53D23003070006) project – funded by European Union – Next Generation EU within the PRIN 2022 program (D.D. 104 - 02/02/2022, Ministero dell'Università e della Ricerca). This manuscript reflects only the authors' views and opinions and the Ministry cannot be considered responsible for them.

References

- [1] H.R. Fernandes, A. Gaddam, A. Rebelo, D. Brazete, G.E. Stan, J.M.F. Ferreira, Bioactive glasses and glass-ceramics for healthcare applications in bone regeneration and tissue engineering, *Materials* 11 (12) (Dec. 2018) 2530, <https://doi.org/10.3390/ma11122530>.
- [2] A. Gocha, L. McDonald, Better bodies with biomaterials: how ceramic and glass contribute to the \$110B global market for implantable bio-materials, *Am. Ceram. Soc. Bull.* 99 (2020).
- [3] M. Montazerian, et al., Glass-ceramics in dentistry: fundamentals, technologies, experimental techniques, applications, and open issues, *Prog. Mater. Sci.* 132 (Feb. 2023) 101023, <https://doi.org/10.1016/j.pmatsci.2022.101023>.
- [4] L.L. Hench, Genetic design of bioactive glass, *J. Eur. Ceram. Soc.* 29 (7) (Apr. 2009) 1257–1265, <https://doi.org/10.1016/j.jeurceramsoc.2008.08.002>.
- [5] U. Pantulap, M. Arango-Ospina, A.R. Boccaccini, Bioactive glasses incorporating less-common ions to improve biological and physical properties, *J. Mater. Sci. Mater. Med.* 33 (1) (Jan. 2022) 3, <https://doi.org/10.1007/s10856-021-06626-3>.
- [6] F. Baino, et al., Processing methods for making porous bioactive glass-based scaffolds—a state-of-the-art review, *Int. J. Appl. Ceram. Technol.* 16 (5) (Sep. 2019) 1762–1796, <https://doi.org/10.1111/ijac.13195>.
- [7] A.A. El-Rashidy, J.A. Roether, L. Harhaus, U. Kneser, A.R. Boccaccini, Regenerating bone with bioactive glass scaffolds: a review of in vivo studies in bone defect models, *Acta Biomater.* 62 (Oct. 2017) 1–28, <https://doi.org/10.1016/j.actbio.2017.08.030>.
- [8] M.-M. Germaini, S. Belhabib, S. Guessasma, R. Deterre, P. Corre, P. Weiss, Additive manufacturing of biomaterials for bone tissue engineering – a critical review of the state of the art and new concepts, *Prog. Mater. Sci.* 130 (Oct. 2022) 100963, <https://doi.org/10.1016/j.pmatsci.2022.100963>.
- [9] K.C.R. Kolan, M.C. Leu, G.E. Hilmas, R.F. Brown, M. Velez, Fabrication of 13-93 bioactive glass scaffolds for bone tissue engineering using indirect selective laser sintering, *Biofabrication* 3 (2) (Jun. 2011) 025004, <https://doi.org/10.1088/1758-5082/3/2/025004>.
- [10] S. Eqtasadi, A. Motealleh, P. Miranda, A. Pajares, A. Lemos, J.M.F. Ferreira, Robocasting of 45S5 bioactive glass scaffolds for bone tissue engineering, *J. Eur. Ceram. Soc.* 34 (1) (Jan. 2014) 107–118, <https://doi.org/10.1016/j.jeurceramsoc.2013.08.003>.
- [11] P. Tesavibul, et al., Processing of 45S5 Bioglass® by lithography-based additive manufacturing, *Mater. Lett.* 74 (May 2012) 81–84, <https://doi.org/10.1016/j.matlet.2012.01.019>.
- [12] F. Baino, J. Dias, M. Alidoost, M. Schwentenwein, E. Verné, Making foam-like bioactive glass scaffolds by vat photopolymerization, *Open Ceramics* 15 (Sep. 2023) 100392, <https://doi.org/10.1016/j.oceram.2023.100392>.
- [13] F. Baino, et al., Digital light processing stereolithography of hydroxyapatite scaffolds with bone-like architecture, permeability, and mechanical properties, *J. Am. Ceram. Soc.* 105 (3) (Mar. 2022) 1648–1657, <https://doi.org/10.1111/jace.17843>.
- [14] L. D'Andrea, et al., Computational models for the simulation of the elastic and fracture properties of highly porous <sc>3D</sc>-printed hydroxyapatite scaffolds, *Int J Numer Method Biomed Eng* 40 (2) (Feb. 2024), <https://doi.org/10.1002/cnm.3795>.
- [15] L.-C. Gerhardt, A.R. Boccaccini, Bioactive glass and glass-ceramic scaffolds for bone tissue engineering, *Materials* 3 (7) (Jul. 2010) 3867–3910, <https://doi.org/10.3390/ma3073867>.
- [16] S.I. Schmitz, et al., Superior biocompatibility and comparable osteoinductive properties: sodium-reduced fluoride-containing bioactive glass belonging to the CaO–MgO–SiO₂ system as a promising alternative to 45S5 bioactive glass, *Bioact. Mater.* 5 (1) (Mar. 2020) 55–65, <https://doi.org/10.1016/j.bioactmat.2019.12.005>.
- [17] D.U. Tulyaganov, M.E. Makhkamov, A. Urazbaev, A. Goel, J.M.F. Ferreira, Synthesis, processing and characterization of a bioactive glass composition for bone regeneration, *Ceram. Int.* 39 (3) (Apr. 2013) 2519–2526, <https://doi.org/10.1016/j.ceramint.2012.09.011>.
- [18] I. Kansal, D.U. Tulyaganov, A. Goel, M.J. Pascual, J.M.F. Ferreira, Structural analysis and thermal behavior of diopside–fluorapatite–wollastonite-based glasses and glass–ceramics, *Acta Biomater.* 6 (11) (Nov. 2010) 4380–4388, <https://doi.org/10.1016/j.actbio.2010.05.019>.
- [19] K. Dimitriadis, K.C. Vasilopoulos, T.C. Vaimakis, M.A. Karakassides, D. U. Tulyaganov, S. Agathopoulos, Synthesis of glass-ceramics in the Na₂O/K₂O–CaO–MgO–SiO₂–P₂O₅–CaF₂ system as candidate materials for dental applications, *Int. J. Appl. Ceram. Technol.* 17 (4) (Jul. 2020) 2025–2035, <https://doi.org/10.1111/ijac.13509>.
- [20] K. Dimitriadis, D. Moschovas, D.U. Tulyaganov, S. Agathopoulos, Development of novel bioactive glass-ceramics in the Na₂O/K₂O–CaO–MgO–SiO₂–P₂O₅–CaF₂ system, *J. Non-Cryst. Solids* 533 (Apr) (2020), <https://doi.org/10.1016/j.jnoncrsol.2020.119936>.
- [21] F. Baino, D.U. Tulyaganov, Z. Kahharov, A. Rahdar, E. Verné, Foam-replicated diopside/fluorapatite/wollastonite-based glass–ceramic scaffolds, *Ceramics* 5 (1) (Mar. 2022) 120–130, <https://doi.org/10.3390/ceramics5010011>.
- [22] A. Schiavi, A. Prato, Evidences of non-linear short-term stress relaxation in polymers, *Polym. Test.* 59 (May 2017) 220–229, <https://doi.org/10.1016/j.polymertesting.2017.01.030>.
- [23] T. Kokubo, H. Takadama, How useful is SBF in predicting in vivo bone bioactivity? *Biomaterials* 27 (15) (May 2006) 2907–2915, <https://doi.org/10.1016/j.biomaterials.2006.01.017>.
- [24] A.L.B. Maçon, et al., A unified in vitro evaluation for apatite-forming ability of bioactive glasses and their variants, *J. Mater. Sci. Mater. Med.* 26 (2) (Feb. 2015) 115, <https://doi.org/10.1007/s10856-015-5403-9>.
- [25] S.-B. Hua, et al., Digital light processing porous TPMS structural HA & akermanite bioceramics with optimized performance for cancellous bone repair, *Ceram. Int.* 48 (3) (Feb. 2022) 3020–3029, <https://doi.org/10.1016/j.ceramint.2021.10.003>.
- [26] M. Liu, Y. Wang, X. Liu, Q. Wei, C. Bao, K. Zhang, Comprehensive review on fabricating bioactive ceramic bone scaffold using vat photopolymerization, *ACS Biomater. Sci. Eng.* 9 (6) (Jun. 2023) 3032–3057, <https://doi.org/10.1021/acsbomaterials.3c00051>.
- [27] Z. Schwartz, B.D. Boyan, Underlying mechanisms at the bone–biomaterial interface, *J. Cell. Biochem.* 56 (3) (Nov. 1994) 340–347, <https://doi.org/10.1002/jcb.240560310>.
- [28] A. Schiavi, E. Fiume, G. Orlygsson, M. Schwentenwein, E. Verné, F. Baino, High-reliability data processing and calculation of microstructural parameters in hydroxyapatite scaffolds produced by vat photopolymerization, *J. Eur. Ceram. Soc.* 42 (13) (Oct. 2022) 6206–6212, <https://doi.org/10.1016/j.jeurceramsoc.2022.06.022>.
- [29] L.J. Gibson, Modelling the mechanical behavior of cellular materials, *Mater. Sci. Eng., A* 110 (Mar. 1989) 1–36, [https://doi.org/10.1016/0921-5093\(89\)90154-8](https://doi.org/10.1016/0921-5093(89)90154-8).
- [30] Q.Z. Chen, I.D. Thompson, A.R. Boccaccini, 45S5 Bioglass®-derived glass–ceramic scaffolds for bone tissue engineering, *Biomaterials* 27 (11) (Apr. 2006) 2414–2425, <https://doi.org/10.1016/j.biomaterials.2005.11.025>.
- [31] F. Baino, E. Fiume, Elastic mechanical properties of 45S5-based bioactive glass–ceramic scaffolds, *Materials* 12 (19) (Oct. 2019) 3244, <https://doi.org/10.3390/ma12193244>.
- [32] L.-E. Monfoulet, et al., The pH in the microenvironment of human mesenchymal stem cells is a critical factor for optimal osteogenesis in tissue-engineered constructs, *Tissue Eng.* 20 (13–14) (Jul. 2014) 1827–1840, <https://doi.org/10.1089/ten.tea.2013.0500>.
- [33] L.L. Hench, Bioactive ceramics, *Ann. N. Y. Acad. Sci.* 523 (1) (Jun. 1988) 54–71, <https://doi.org/10.1111/j.1749-6632.1988.tb38500.x>.
- [34] A. Nommeots-Nomm, P.D. Lee, J.R. Jones, Direct ink writing of highly bioactive glasses, *J. Eur. Ceram. Soc.* 38 (3) (Mar. 2018) 837–844, <https://doi.org/10.1016/j.jeurceramsoc.2017.08.006>.